PHYSICAL REVIEW FLUIDS **7**, 093601 (2022)

Editors' Suggestion

Free rising skirt bubbles

Dominique Legendre
Institut de Mécanique des Fluides de Toulouse, Université de Toulouse, CNRS, INPT, UPS,
31400 Toulouse, France

(Received 10 March 2022; accepted 26 July 2022; published 12 September 2022)

The motion of a free rising skirt bubble is studied using direct numerical simulation covering the range of Eötvös (Bond) and Morton numbers where they can be observed. We investigate the skirt bubble motion (terminal velocity and drag), the flow field structure (inside the skirt film, around the bubble, and inside the gas film that forms the skirt) as well as the geometrical characteristics of the skirt (both length and thickness). A unified relation for the terminal velocity (and drag force) is provided for all bubble shapes (dimple, skirt, and spherical cap bubbles) when considering Eötvös numbers (based on bubble diameter) larger than 100. The velocity field around and inside the bubble is investigated resulting in the clarification of the wake structure with a major difference with the flow deduced from experimental observations during the 1970s. The numerical simulations reveal that only one recirculation is observed inside the bubble while two vortices are highlighted in the wake. We confirm that a parallel Poiseuille flow develops inside the skirt film resulting in an intense vorticity field. Original modeling is improved with a Reynolds correction that makes possible the prediction of the film thickness in very good agreement with the only experimental value available in the literature. Our simulations combined with experimental observations suggest the existence of a maximum value for the skirt length.

DOI: 10.1103/PhysRevFluids.7.093601

I. INTRODUCTION

For large bubbles rising in a viscous fluid, a thin layer of gas, commonly referred to as a "skirt," can be observed issuing from the rim of bubbles. It seems that the skirt phenomenon was first reported for drops by Thomson and Newall [1] who observed a "thin cylindrical part at the edge" of drop made of a solution of oleate of soda falling into paraffin oil. According to experimental observations, the appearance of skirts requires a sufficiently viscous continuous phase. A criterion for the skirt formation has been proposed considering that the balance between the surface tension and the normal viscous stress becomes impossible [2]. After its formation a skirt can grow to a stable length or can become unstable and shed small fragments or large volumes. Guthrie [3] and then Guthrie and Bradshaw [4] proposed a simplified approach for calculating the skirt thickness δ considering a parallel vertical and fully developed flow inside the skirt. Wairegi [5] and then Bhaga [2] extended the theory proposed by Guthrie and Bradshaw [4] to the case of drops and conducted additional experiments. More recently, Ray and Prosperetti [6] considered the effect of the viscous boundary layer that develops along the surface. However, a significant discrepancy between the proposed models and the experiments still needs to be clarified. Most of the experimental studies have focused on skirt drop. As a consequence, few information, in particular for skirt thickness and length, are available for skirt bubble, i.e., when both the bubble density ρ_B and viscosity μ_B are much smaller than the density ρ_L and viscosity μ_L of the external fluid. In such system, a typical thickness for the skirt film is around 50 μm making experimentation difficult. In such conditions, numerical simulation is very useful for conducting bubble skirt investigations because of the total control of both the parameters and the condition of bubble generation with a nonintrusive measurement of the flow inside the skirt. Surprisingly, few numerical works have focused on skirt bubble dynamics. Most of them report only bubble or drop skirt shapes and corresponding terminal velocity [7]. Ohta and Sussman [8] discussed the effect of the density and viscosity ratio on the skirt and outlined the importance of the internal skirt density on the development of the skirt. Most of the numerical studies are using the skirt bubbles shape as a reference benchmark case for code performance comparison and validation [9–13] (see Ohta and Sussman [8] for a review of the numerical methods used). Thus, a systematic numerical investigation has not yet been proposed to conduct a deep investigation of skirt bubble dynamics, with a detailed inspection of rising velocity (and drag force) as well bubble skirt characteristics. In particular the parameters that control bubble skirt thickness and length still need to be clarified. This is the motivation of this work, which focuses on the "bubble" skirt case.

The paper is organized as follows. First, we present the numerical method, the numerical setup designed for the study, and the specific tests made for the bubble skirt configuration. Then we discuss the shape of bubble when varying both the Eötvös (Bond) and Morton number in the region of the phase diagram where skirt bubbles are expected to be observed according to Clift *et al.* [15] and Tripathi *et al.* [14]. The terminal velocity and drag force of a skirt bubble but also a spherical cap and dimple bubble are discussed. We finally investigate the specific characteristic of a skirt bubble, with a particular attention to the skirt film.

II. PROBLEM STATEMENT AND NUMERICAL SOLVER

We consider a spherical bubble of diameter d, density ρ_B, and dynamic viscosity μ_B released from rest in a Newtonian liquid of density ρ_L and dynamic viscosity μ_L. Due to the gravity g, the bubble rises in the liquid and deforms if the surface tension effects are weaker than hydrostatic, inertia, and viscous effects at the bubble surface. The aim of this work is to focus on stable skirt bubbles. Considering that both $\rho_B \ll \rho_L$ and $\mu_B \ll \mu_L$ (the "bubble" case), such a problem is controlled by two nondimensional numbers. The identification of the range of parameter for the observation of a stable skirt bubble can be achieved by varying the Eötvös (Bond) number $\mathrm{Eo} = \rho_L g d^2/\sigma$ and the Morton number $\mathrm{Mo} = g\mu_L^4/\rho_L\sigma^3$, where σ is the surface tension. We also introduce the bubble Reynolds number $\mathrm{Re} = \rho_L U_B d/\mu_L$, the bubble capillary number $\mathrm{Ca} = \mu_L U_B/\sigma$, and the Galileo number $\mathrm{Ga} = \rho_L g^{1/2} d^{3/2}/\mu_L$.

The numerical simulations reported in this work are performed with the Level Set solver [16–18] developed in the JADIM code [9,19]. The two fluids are considered as Newtonian and incompressible with no phase change. Under isothermal conditions and in the absence of any surfactant, the surface tension is constant and uniform at the interface between the two fluids. In such a case, the velocity field U and the pressure P satisfy the classical one-fluid formulation of the Navier-Stokes equations:

$$\nabla \cdot U = 0, \tag{1}$$

$$\rho\left(\frac{\partial U}{\partial t} + U \cdot \nabla U\right) = -\nabla P + \nabla \cdot \Sigma + \rho g + F_\sigma, \tag{2}$$

where $\Sigma = \mu[\nabla U + (\nabla U)^T]$ is the viscous stress tensor, g is the gravity, and F_σ is the capillary contribution:

$$F_\sigma = \sigma \nabla \cdot n\, n \delta_I, \tag{3}$$

where n denotes by arbitrary choice the unit normal of the interface going out from the drop and δ_I is the Dirac distribution associated with the interface. The Level Set function satisfies the advection equation

$$\frac{\partial \phi}{\partial t} + \nabla \cdot (\phi U) = 0. \tag{4}$$

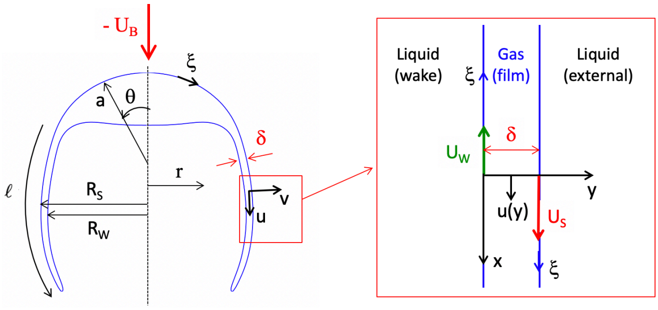

FIG. 1. Variables used for the skirt bubble description in a referential frame moving with the bubble. a is the front curvature, θ the polar angle taken from the vertical axis of symmetry, r the radial distance to the symmetry axis, δ the skirt thickness, ℓ the skirt length, ξ the interfacial curvilinear coordinate, and R_S and R_W the mean radius of curvature of the skirt internal and external surface, respectively.

The interface corresponds to the isovalue $\phi = 0$, the gas phase to $\phi > 0$, and the liquid phase to $\phi < 0$. In order to keep the Level Set function as close as possible to a signed distance function, a redistancing procedure is applied [20]:

$$\frac{\partial \phi}{\partial \tau} + \mathrm{sgn}(\phi)(|\nabla \phi| - 1) = 0. \tag{5}$$

The density and viscosity are deduced by linear interpolation from the Level Set function ϕ in each computational cell:

$$\rho = H(\phi)\rho_B + [1 - H(\phi)]\,\rho_L, \tag{6}$$

$$\mu = H(\phi)\mu_B + [1 - H(\phi)]\,\mu_L, \tag{7}$$

where the approximation $H(\phi)$ of the Heaviside function is given by

$$H(\phi) = \begin{cases} 0 & \text{if } \phi < -\varepsilon, \\ 0.5\left[1 + \frac{\phi}{\varepsilon} + \frac{1}{\pi}\sin\left(\frac{\pi\phi}{\varepsilon}\right)\right] & \text{if } |\phi| \leqslant \varepsilon, \\ 1 & \text{if } \phi > \varepsilon, \end{cases} \tag{8}$$

where $\varepsilon = \sqrt{2}\Delta x$ is half the numerical thickness of the interface.

The system of equations (1)–(4) is discretized using the finite volume method. Time advancement is achieved through a third-order Runge-Kutta method. Equations (4)–(5) for ϕ are solved using a WENO5 scheme, and the Hamiltonian fluxes are calculated with a Godunov operator. Incompressibility is satisfied at the end of each time step though a projection method.

The parameters used in this paper to describe the skirt shape and velocity field are presented in Fig. 1.

A. Computational domain and grid tests

We consider an axisymmetric bubble shape allowing the simulation to be performed using axisymmetric conditions with the symmetry axis parallel to gravity. The computational domain D is shown in Fig. 2. The simulations are performed in the frame of reference moving with the bubble. As a consequence the following boundary conditions are considered at each time step n: the inlet velocity $U_\infty^n = -U_B^n$ on the north face, axisymmetric conditions on the west boundary, a no sliding condition on the east boundary, and an exit condition on the south boundary. The bubble

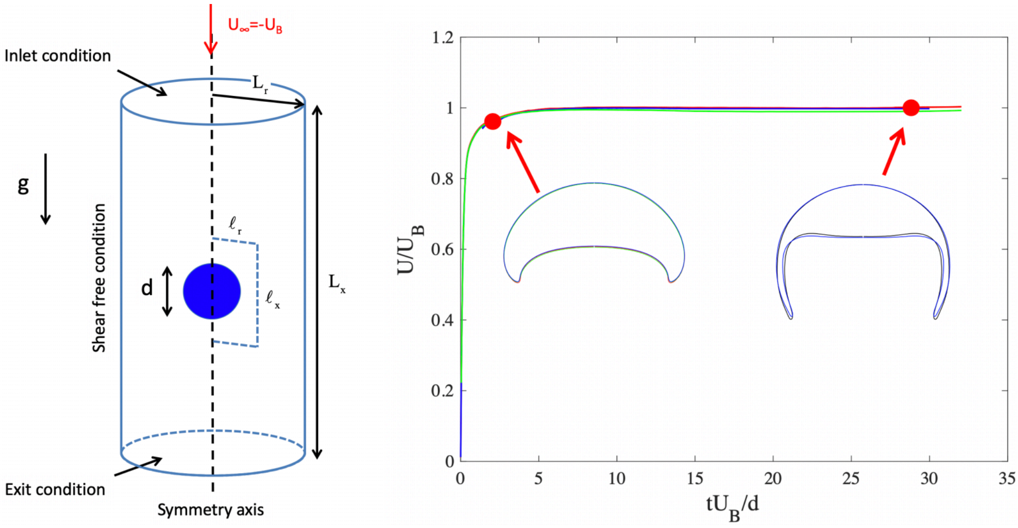

FIG. 2. (Left) Computational domain D and grid parameters in the frame of reference moving with the bubble. (Right) Effect of the grid refinement for the case (Eo = 330, Mo = 100) on the bubble velocity and shape for d/Δ= 125 (green), 250 (red), and 500 (blue). The bubble velocity is normalized with the terminal velocity obtained with the thinner grid GRID3.

rising velocity evolution with time is calculated as

$$U_B^{n+1} = U_B^n + \frac{1}{\vartheta_B} \int_D H(\phi) U^n \, d\vartheta, \tag{9}$$

where U^n is the velocity field calculated at time n and ϑ_B is the bubble volume.

The vertical length of the computational domain is noted L_x and its radial expansion is L_r. The specific challenge of simulating skirt bubble as addressed in this work resides in the ability to capture with a good accuracy the motion of the gas inside the skirt film. In order to save CPU resources, only a region ($\ell_x = 2.5d \times \ell_r = 1.25d$) close to the bubble is refined, and the grid is progressively increased from this region following a geometrical series in both the radial and vertical directions. Typically the ratio between two successive cells is less than 1.1 for all the grids considered. In the refined zone the same grid spacing is used along the vertical and radial direction, $\Delta = \ell_x/n_x = \ell_r/n_r$ where n_x and n_r are the corresponding number of nodes. Different grids have been tested in order to ensure that results are grid independent and to avoid domain confinement. The grid parameters are shown in Table I for the grids GRID1, GRID2, and GRID3 corresponding to d/Δ= 125, 250, and 500, respectively. The corresponding evolution of the velocity is reported in Fig. 2, and two typical shapes obtained for the three grids are compared. As shown the difference between the three grids can not be distinguished in the figure, in particular when considering the bubble skirt. The film

TABLE I. Grid characteristics and number of cells per diameter and inside the skirt. The number of cells inside the skirt is given for the case (Eo = 330, Mo = 100).

Name	$L_x/d \times L_r/d$	$N_x \times N_r$	$\ell_x/d \times \ell_r/d$	$n_x \times n_y$	d/Δ	δ/Δ
GRID1	35 × 5	400 × 200	2.5 × 1.25	300 × 150	125	6.4
GRID2	35 × 5	700 × 350	2.5 × 1.25	600 × 300	250	13.8
GRID3	35 × 5	1300 × 650	2.5 × 1.25	1200 × 600	500	25.6

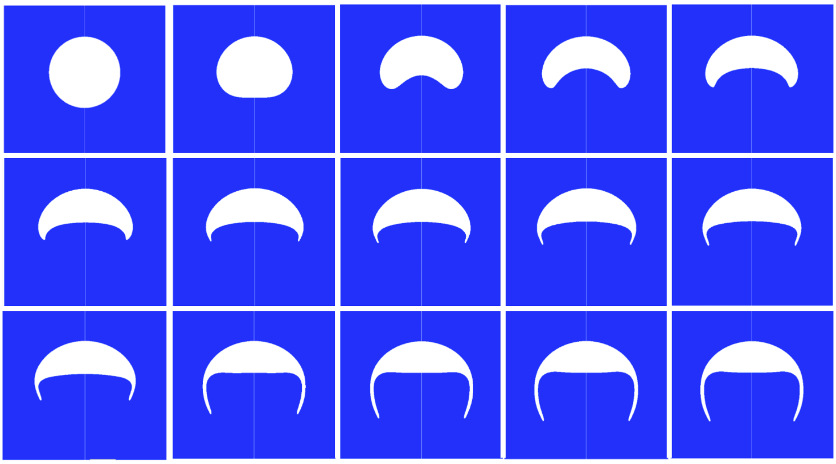

FIG. 3. Bubble shape evolution with time for Eo = 330 and Mo = 100. At $t = 0$ the initial shape is a sphere. The normalized times tU_B/d_B are from left to right: first row (initial bubble deformation) 0, 0.43, 0.86, 1.28, 1.71; second row (onset of the skirt) 2.14, 2.56, 2.99, 3.42, 3.85; last row (skirt elongation) 4.27, 8.55, 12.8, 17.1, 21.4.

is described by 6.5, 13, and 26 cells when increasing the refinement from GRID1 to GRID3. The simulations reported in the following were conducted with GRID2 corresponding to $d/\Delta = 250$.

III. SKIRT AND DIMPLED/CAP BUBBLES

The phase diagram (Eo, Mo) inspection for skirt bubble identification is conducted by varying the Morton number Mo for a fixed Eötvös Eo number and by varying the Eötvös number for a fixed Morton number. The viscosity ratio and density ratio between the bubble and the liquid are maintained constant and close to the air/water system: $\mu_B/\mu_L = 0.018$ and $\mu_B/\mu_L = 0.0014$. Eo and Mo numbers are varying in the range 100 to 750 and 0.01 to 10 000, respectively. From the bubble release at zero velocity, the time evolution of the rising velocity is similar for all the considered cases to the one reported in Fig. 2 for Eo = 330 and Mo = 100. Corresponding bubble shapes at different times are reported in Fig. 3 revealing three typical stages in the skirt bubble formation. Starting from a spherical shape, we first observe that the bubble rear is deformed and the curvature is inverted (first row). Then a toroidal small appendix appears at the bubble surface (second row), and it progressively develops to form a skirt (last row). For the first image of the second row in Fig. 3 the bubble has already reached 96% of its terminal velocity, indicating that the bubble reaches first its terminal velocity with a shape close to a dimple bubble. Then the skirt develops and the length of the skirt increases and stabilizes around $tU_B/d_B = 30$ for the case shown in Fig. 3. Similar orders of magnitude for these characteristic times are observed for all the skirt bubbles considered here. Clearly the bubble relaxation time to reach the terminal velocity is much smaller than the characteristic time for the skirt formation process.

Some stabilized bubble shapes observed when varying both Eo and Mo are reported in Fig. 4. A minimum Eötvös number (between 100 and 200) is required to observe skirt bubbles. When decreasing the Morton number, dimple bubble deformation is increased and skirt bubbles are observed. Below a threshold Morton number, skirt bubbles are becoming unstable and are indicated using an asterisk. In Fig. 4 we recognize three of the four typical shapes reported by Bhaga [2]: the spherical shape, oblate shape, and straight skirt shape. The prolate shape has not been observed here for the conditions corresponding to $\mu_G/\mu_L \ll 1$ and $\rho_G/\rho_L \ll 1$.

According to Fig. 4 bubbles can be classified into the following groups for the range of parameter investigated: stable skirt bubbles, dimpled bubbles, spherical cap bubbles, and unstable skirt

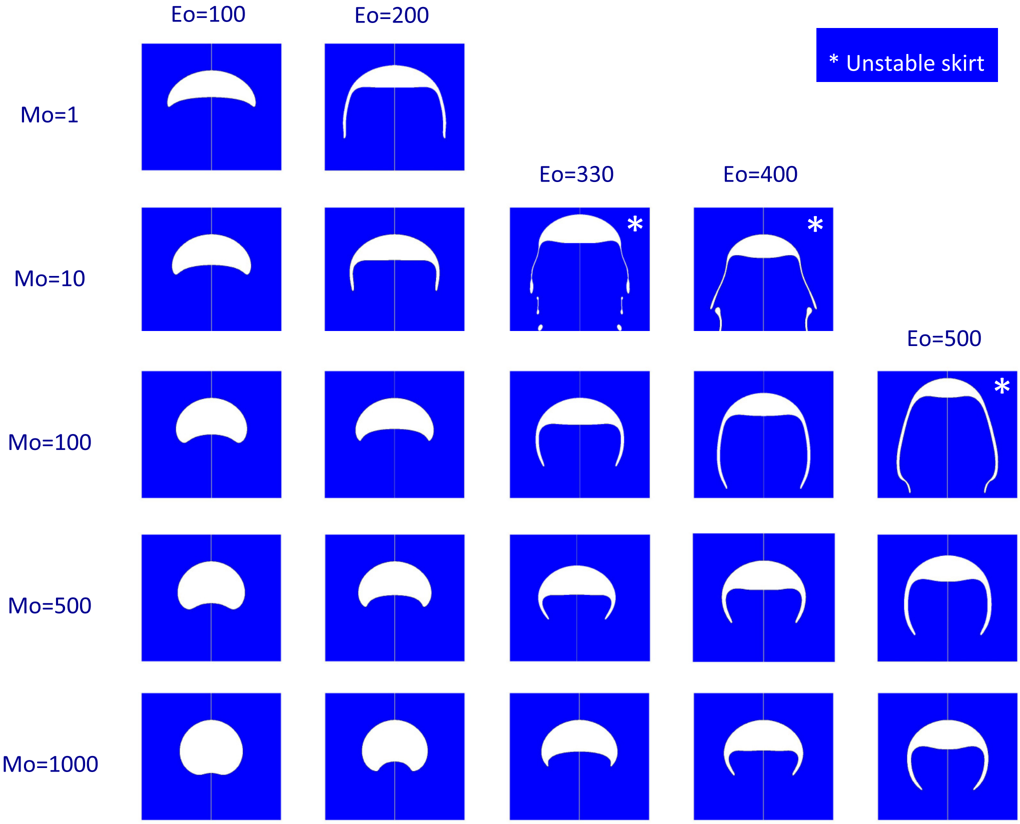

FIG. 4. Bubble shapes at steady state when varying both Eo and Mo. Asterisk indicates unstable skirt cases.

bubbles. The corresponding families are shown in Fig. 5 using the diagram Eo-Re deduced from experiments by Clift *et al.* [15] and the diagram Ga-Eo proposed by Tripathi *et al.* [14] based on 3D numerical simulations. The map corresponding to dimple cap and skirt bubble are consistent with both references. However, the transition between stable and unstable skirt bubble does not clearly match the transition reported by Tripathi *et al.* [14]. The difference maybe explained because we are conducting axisymmetric simulations while 3D simulations were reported in Tripathi *et al.* [14]. Note that, concerning the transition between skirt and dimpled bubbles, Tripathi *et al.* [14] do not report the dimpled shape, but the transition reported here from dimpled bubble to ellipsoidal bubble is in agreement with their transition from skirt bubble to ellipsoidal bubble.

The onset of the skirt has been discussed in Wairegi [5]. Considering the creeping flow solution on both sides, the bubble corner and balancing normal stress and surface tension, Wairegi [5] proposed a relation between the capillary number (also called the "skirt number") and the corner shape characterized by the angle α (see Fig. 5.1 in Wairegi [5]). The transition between dimple bubble and skirt bubble was reported in a Ca-Re diagram, and experimental observations of Wairegi [5] indicate that a skirt is observed for Re $\geqslant 4$ and Ca $\geqslant 1$. Based on additional experimental data, Clift *et al.* [15] proposed the following relation for this transition:

$$\mathrm{Ca} = 2.32 + \frac{11}{(\mathrm{Re} - 9)^{0.7}}. \tag{10}$$

Our simulations are compared to relation (10) in the Ca-Re diagram reported in Fig. 6. The condition to observe a skirt bubble in our simulations is consistent with the experimental observations of

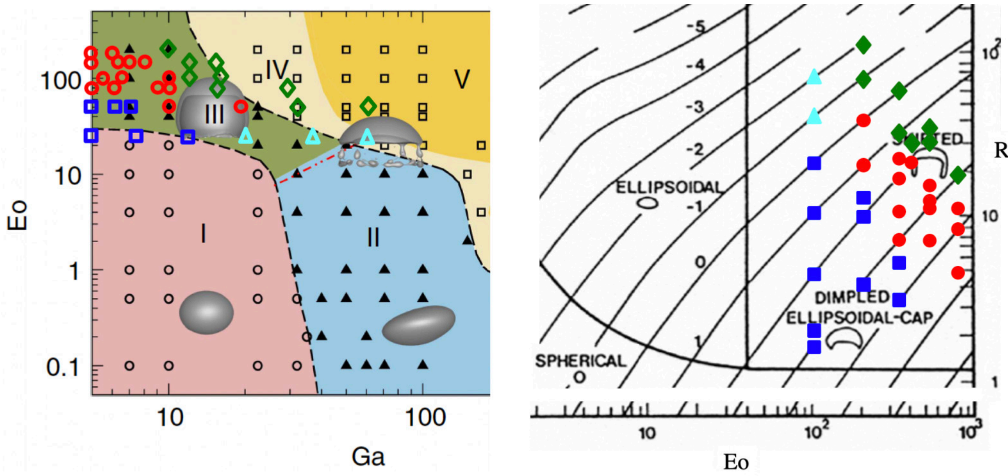

FIG. 5. Bubble shapes reported in the diagrams (left) ($\mathrm{Ga} = \rho_L \sqrt{gR}R/\mu_L$, $\mathrm{Eo} = \rho_L g R^2/\sigma$) from Tripathi *et al.* [14] and (right) ($\mathrm{Eo} = \rho_L g d^2/\sigma$, $\mathrm{Re} = \rho_L U_B d/\mu_L$) from Clift *et al.* [15]. This study: ○ skirt bubble, □ dimpled bubble, ◊ unstable skirt bubble, and △ spherical cap bubble.

Wairegi [5]. As shown, an agreement is observed around $\mathrm{Re} = 10$, while in experiments skirt bubbles have been observed in a smaller domain for both larger and smaller Reynolds numbers. This may be due to both the experimental difficulty of identifying the skirt formation and the use of 2D axisymmetric conditions in our simulations that may force the skirt stability, extending in an artificial way the domain for their observation. Based on our simulations, the transition from dimple bubble to skirt bubble is described by a simple power law of the form

$$\mathrm{Ca} \approx 70\mathrm{Re}^{-1} \tag{11}$$

corresponding to a constant value for the Weber number $\mathrm{We} = 70$ as shown in the insert of Fig. 6. The transition from stable to unstable skirt deduced from the numerical results is reported in

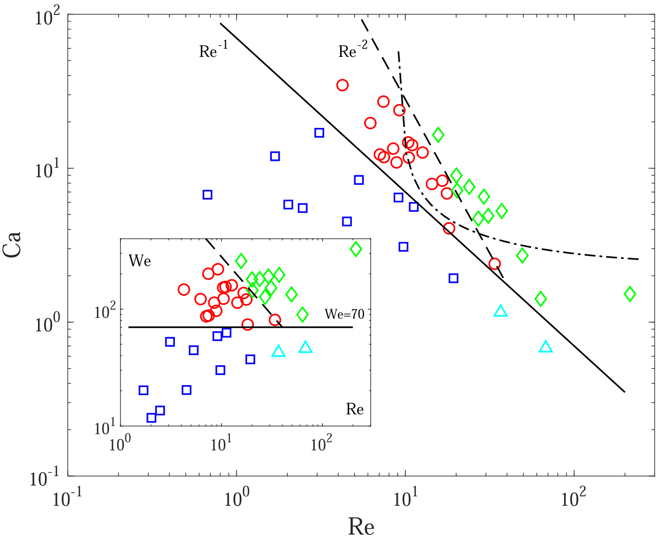

FIG. 6. Bubble shape in the diagram Ca-Re. Insert diagram We-Re. ○ Skirt bubble, □ dimpled bubble, ◊ unstable skirt bubble, △ spherical cap bubble. — $\mathrm{We} = \mathrm{CaRe} = 70$, – – – $\mathrm{Ca} = 2800\mathrm{Re}^{-2}$, – · – relation (10).

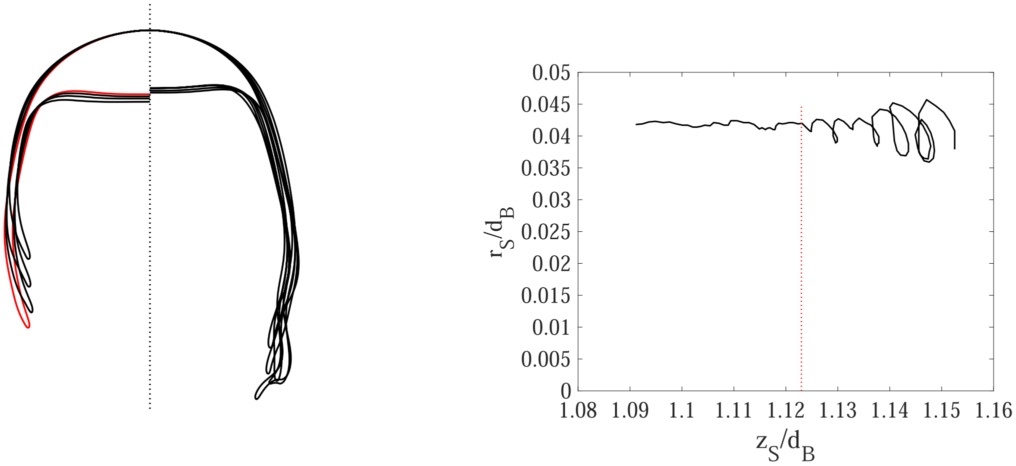

FIG. 7. Shape evolution of an unstable skirt bubble (Eo = 500, Mo = 100, and Re = 20.0). (Left) Bubble shape showing the skirt development up to the instability onset at time $tU_B/d_B = 8.08, 10.8, 13.5, 16.2$ (in red) on the left side, and first skirt oscillations due to the stability development at time $tU_B/d_B = 18.9, 24.2, 26.9, 29.6, 32.2$ on the right side. (Right) Evolution of the skirt tip position. The normalized radial position of the tip z_S/d_B is reported as a function of the normalized vertical position z_S/d_B. The vertical red dash line corresponds to the beginning of the skirt instability.

Fig. 6. It can be simply described by Ca $\approx 2800\text{Re}^{-2}$ corresponding to the equivalent relation We $\approx 2800\text{Re}^{-1}$.

The bubble shape before and after the stability development is shown in Fig. 7 for the case Eo = 500, Mo = 100 corresponding to Re = 20.0. The terminal velocity and thus the bubble Reynolds number stabilizes before the development of the instability that seems to happen when the skirt has reached a critical length. Figure 7 reports the skirt shape evolution up to the instability as well as right after the instability development. As shown the instability starts at the skirt tip and then the instability develops. Figure 7 also reports the corresponding skirt tip position evolution. The vertical position z_S of the skirt tip is reported as a function of its radial position r_S. The observed instability frequency f normalized using the bubble diameter and rising velocity gives a Strouhal number value St $= fd/U \approx 0.33$. The evolution of the normalized frequency St is reported in Fig. 8 as a function of the Reynolds number for different unstable skirts. Both the Morton number and the

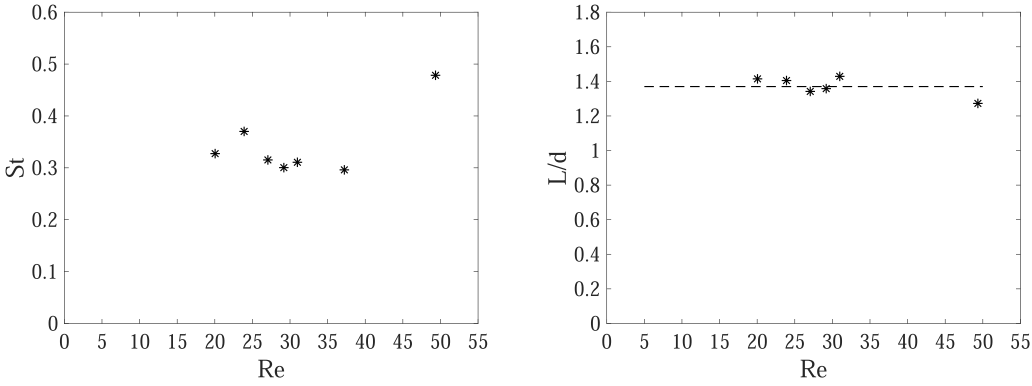

FIG. 8. (Left) Normalized frequency St as a function of the bubble Reynolds number. (Right) Normalized skirt length when the instability develops as a function of the bubble Reynolds number. — — $\ell = 1.37d$.

Bond number are varied. As shown, the Strouhal number is almost constant in the range 0.3–0.4. The skirt length when the instability starts to develop at the skirt tip is reported in Fig. 8. This plot outlines that the skirt instability seems to appear when the skirt has reached a critical skirt length $\ell = 1.37d$ reported using a dashed line. This value is remarkable and does not seem to depend on the physical properties as well as on the bubble Reynolds number. The skirt length is discussed in more detail at the end of the paper. Note that the transition between stable and unstable bubble skirt has to be considered carefully since the flow is forced to be axisymmetric in our simulations and 3D effects are expected to have an important influence on both the apparition and the development of skirt instabilities. A detailed characterization of the transition between stable and unstable skirt would require 3D simulations. This is out of the scope of the present work, which aims to focus on the dynamics of stable skirt bubbles.

IV. TERMINAL VELOCITY AND DRAG FORCE

In this section we consider the rising speed for all the simulated bubbles, i.e., for skirt bubbles, dimpled bubbles, and spherical cap bubbles. As will be shown, a unified relation for the terminal velocity (and drag force) is proposed to describe the motion of any bubble having an Eötvös number larger than 100.

A. Terminal velocity

According to the (Eo-Re) diagram [15], the skirt bubble regime is bounded by the spherical cap bubble regime when increasing the bubble Reynolds number. Davies and Taylor [21] determined the terminal rising velocity of a spherical cap bubble by balancing the dynamic pressure given by the potential flow around a sphere $9\rho_L U_B^2 \sin^2\theta$ with the liquid hydrostatic pressure variation $\rho_L g a(1-\cos\theta)$ at the bubble nose, where a is the radius of the spherical cap and θ is here the angle made from the stagnation point (see Fig. 1). The limit for $\theta \to 0$ gives the rising velocity:

$$U_B = \frac{2}{3}\sqrt{ga}. \tag{12}$$

This relation is expected to be valid for $\mathrm{Re} \gg 1$, $\mathrm{We} \gg 1$, and $\mathrm{Eo} \gg 1$ since the flow is assumed to be potential at the bubble front, and surface tension is considered to be negligible compared to both inertia and gravity. For a spherical cap, the front curvature a can be related to the bubble diameter as $a = c(\mathrm{Re})d$. In fact, $c(\mathrm{Re})$ depends on the angle θ_c made by the cap that itself depends on the Reynolds number. In the limit of large Reynolds number the cap angle reaches a constant value of $\theta_c \approx 50^\circ$ corresponding to $c(\mathrm{Re}) = 1.14$, so that the velocity can be simply linked to the bubble diameter as

$$U_B = 0.707\sqrt{gd}. \tag{13}$$

From the simulated shapes the bubble front curvature a has been determined by fitting the surface by a spherical cap. Figure 9 shows that the normalized curvature a/d follows a unique evolution with Re for all the shapes considered here. a/d has a monotonic evolution from the spherical shape where $a = d/2$ to the spherical cap regime discussed above where $a = 1.14d$. As shown in Fig. 9, the relation between the cap radius a and the bubble diameter d can be fitted to

$$a = \frac{12 + 1.14\,\mathrm{Re}^{1.25}}{24 + \mathrm{Re}^{1.25}}\,d. \tag{14}$$

The evolution of the normalized rising velocity $U_B/(gd)^{1/2}$ is reported as a function of Re in Fig. 10. The evolution of $U_B/(gd)^{1/2}$ tends at large Re to relation (13) valid for a spherical cap bubble. For lower Reynolds numbers a different trend is observed. At zero Reynolds number the shape of any fluid particle rising in an other fluid is a sphere [22], so in the limit $\mathrm{Re} \to 0$ the Hadamard-Ribzinsky drag force of a spherical bubble [23,24] $2\pi\mu_L d U_B$ is expected. When

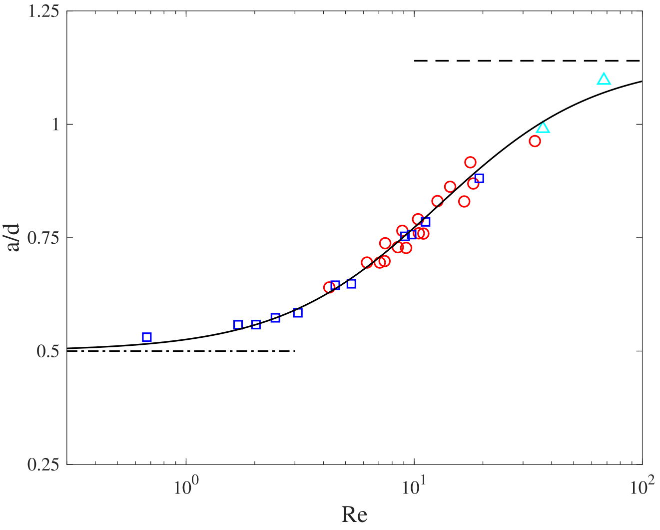

FIG. 9. Evolution of the normalized front curvature a/d as a function of the bubble Reynolds number. □ dimple bubble, ○ skirt bubbles, △ spherical cap. — relation (14), — — $a = 1.14d$ (spherical cap), — · — $a = d/2$ (sphere).

balanced with buoyancy we obtain the terminal rising velocity $U_B = \rho_L d^2 g/12\mu_L$, which can also be expressed under the form

$$U_B = \left(\frac{\text{Re}}{12}\right)^{1/2} \sqrt{gd}. \tag{15}$$

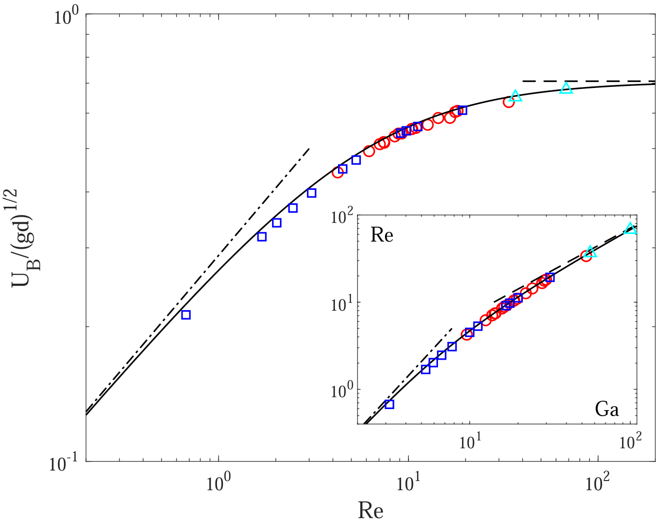

FIG. 10. Bubble terminal velocity U_B normalized by $(gd)^{1/2}$ as a function of Re. □ Dimple bubble, ○ skirt bubbles, △ spherical cap. — relation (16), — — relation (13), — · — relation (15). Insert: Bubble Reynolds number as a function of Galileo number. — relation (17), — — Re = 0.707 Ga, — · — Re = $\text{Ga}^2/12$.

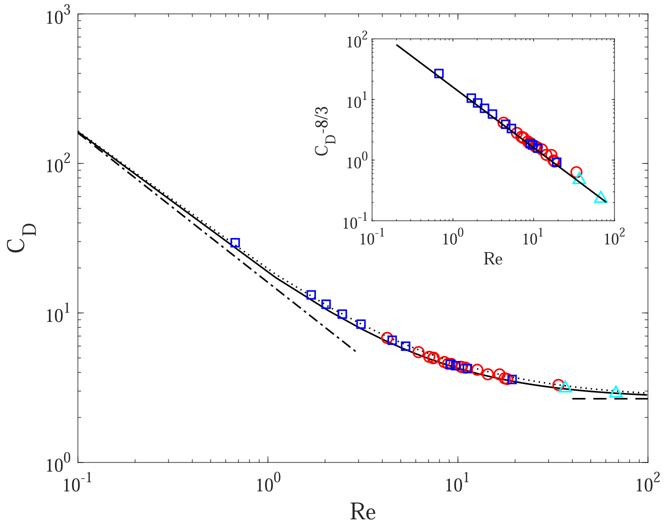

FIG. 11. Drag coefficient C_D as a function of Re. □ dimple bubble, ○ skirt bubbles, △ spherical cap. Insert: Evolution of $C_D - 8/3$. $- \cdot -$ $C_D = 16/\mathrm{Re}$ [23,24], — relation (19), $\cdots$ $C_D = [(2.67)^{0.9} + (16/\mathrm{Re})^{0.9}]^{1/0.9}$ [26], $--$ $C_D = 8/3$ [21].

As shown in Fig. 10 this relation is indeed the correct trend in the limit of vanishing Reynolds numbers. Finally, from relations (13) and (15) the following expression for the rising velocity is formed:

$$U_B = \left(2 + \frac{12}{\mathrm{Re}}\right)^{-1/2} \sqrt{gd}. \tag{16}$$

This relation is able to describe the evolution of the velocity of any bubble (dimple, skirt, and spherical cap) for the range of Eötvös number considered here (Eo $\geqslant$ 100). Relations (13) and (15) can be used to express the bubble Reynolds number Re as a function of the Galileo number Ga [25], $\mathrm{Re} = 0.707\ \mathrm{Ga}$, and $\mathrm{Re} = \mathrm{Ga}^2/12$, respectively. From Eq. (16), the normalized bubble velocity expressed using the Reynolds number can be expressed as a function of the *a priori* known Galileo number as

$$\mathrm{Re}\left(2 + \frac{12}{\mathrm{Re}}\right)^{1/2} = \mathrm{Ga}. \tag{17}$$

The Reynolds number is reported as a function of the Galileo number in the insert of Fig. 10. As observed relation (17) provides a very good description of the numerical results with a quadratic dependence of Re with Ga at low Re and a linear dependence of Re with Ga at high Re.

B. Drag force

We now consider the drag force experienced by a skirt bubble. Balancing the drag force $F_D = C_D \pi d^2 \rho_L U_B^2/8$ with buoyancy $\rho_L g \pi d^3/6$, we obtain the classical relation used to determine the drag coefficient from the rising velocity

$$C_D = \frac{4}{3}\frac{gd}{U_B^2}. \tag{18}$$

The evolution of the drag coefficient C_D is reported in Fig. 11. For comparison all the simulated cases are again shown. Considering the above results observed for the velocity evolution, the drag coefficient tends at large Reynolds number to the drag for spherical cap $C_D = 8/3$ [21]. A detailed inspection of the evolution of C_D (see insert of Fig. 11), reveals that $C_D - 8/3$ is found to follow in a very satisfactory way the evolution $16/\mathrm{Re}$ corresponding to the Hadamard-Ribzinsky drag coefficient for a spherical bubble. Finally, the evolution of the drag coefficient for all the bubble shapes (dimpled/spherical cap and skirt) is satisfactorily described using

$$C_D = \frac{8}{3} + \frac{16}{\mathrm{Re}}. \tag{19}$$

Relation (19) is in very good agreement with the relation $C_D = [(2.67)^{0.9} + (16/\mathrm{Re})^{0.9}]^{1/0.9}$ proposed by Bhaga and Weber [26] to fit their experimental data of rising bubble for Morton number $\mathrm{Mo} > 10^{-3}$. Obviously, relations (19) and (16) provide the same information since they are connected by relation (18). Note that this relation was proposed in Clift *et al.* [15] for the evolution of the drag force from spherical bubbles to spherical cap bubbles. We show that it can also be applied to skirt bubbles, i.e., for Eötvös number larger than 100.

A remarkable unique behavior for the bubble rising velocity (and drag force) is observed for all the bubble shapes considered, dimple, skirt, and spherical cap. As outlined by Ohta and Sussman [8] for drops, the presence of a skirt does not change the rising motion behavior. A similar result is found here for bubbles. As observed for a spherical cap bubble, the rising velocity of a skirt bubble is mainly controlled by the flow on the front part of the bubble. The skirt is developing encapsulating the vortex that develops in the bubble wake.

V. SKIRT DESCRIPTION

Different models have been proposed to describe the skirt thickness, and they mostly differ from the assumption made concerning the velocities on both sides of the skirt interface. Model validation with experiments is very challenging because of the experimental difficulty in characterizing the skirt. In particular, because of the skirt curvature and thickness, optical reflections induce a strong perturbation of the measurement. However, skirt model development and their validation require a clear understanding of the velocity field structure, around and inside the skirt. This is the objective of the first part of this section. Then we propose a detailed description of the skirt film characteristics such as its thickness and length.

The parameters used to describe the skirt are reported in Fig. 1. The interfacial curvilinear coordinate ξ is defined along the bubble surface and is varying from the front stagnation point where $\xi = 0$ up to its maximum $\xi = \xi_{\max}$ located at the rear of the bubble inside the skirt. The value of $\xi_{\max}$ depends on how much the bubble deforms and in particular on how long the skirt is. As a reference, $\xi_{\max}/d = \pi/2 \approx 1.57$ for a sphere.

A. Interfacial velocity

We report in Fig. 12 the interfacial bubble velocity U_ξ as a function of the curvilinear coordinate ξ. U_ξ is shown from the front stagnation point ($\xi = 0$) to the rear of the bubble ($\xi = \xi_{\max}$). Four cases are reported in Fig. 12 in order to cover the range of parameters considered and in particular the different observed skirt shapes: bubble with a small skirt [Fig. 12(a)], a circular skirt [Fig. 12(b)], a long skirt [Fig. 12(c)], and an opened skirt [Fig. 12(d)]. These four cases are representative of all the cases considered, and all show a very similar interface velocity distribution. To guide the description, symbols for specific positions are located at the bubble surface and reported on the velocity plot. As observed, U_ξ is found to be positive all along the interface with a minimum value $U_\xi = 0$ at the skirt front and rear but also at the skirt tip. From $\xi = 0$, U_ξ increases linearly with ξ and reaches a maximum velocity (symbol $\circ$) very close to the beginning of the skirt on the external surface. Then U_ξ decreases on the external side of the gas film. U_ξ cancels at the tip ($\triangledown$) and then increases again to reach a maximum inside the skirt ($*$) almost before the inside start of the skirt, and finally U_ξ reaches zero on the symmetry axis. The evolution of U_ξ at both the top and rear of the bubble is varying linearly with ξ corresponding respectively to evolutions of the form $U_\xi \approx U_B\xi/d \approx U_B \sin\theta$

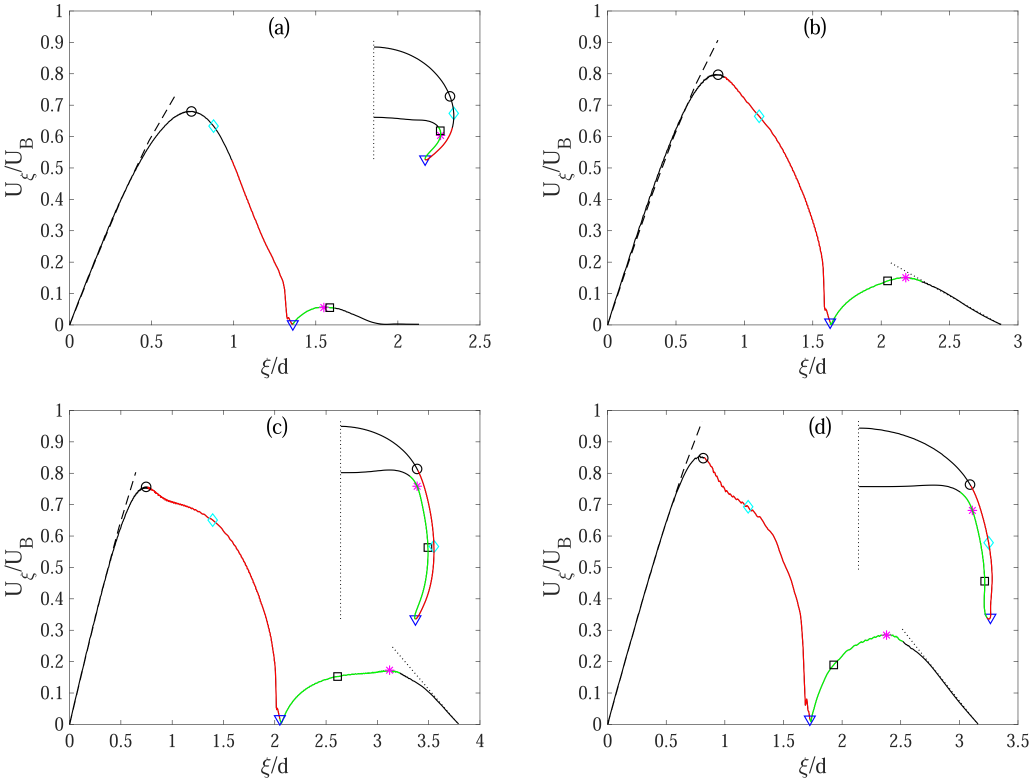

FIG. 12. Tangential velocity U_ξ at the bubble surface as a function of the interface curvilinear length ξ as defined in Fig. 1. U_ξ is defined positive in the direction of ξ. The external (resp. internal) interfacial skirt velocity U_W (resp. U_S) is plotted in red (resp. green). — — — relation (20) with adjusted values for C_f, $\cdots$, $U_\xi \approx U_B r$. (a) $\mathrm{Eo} = 500$ and $\mathrm{Mo} = 5000$ ($\mathrm{Re} = 6.2$ and $C_f = 0.915$); (b) $\mathrm{Eo} = 330$ and $\mathrm{Mo} = 100$ ($\mathrm{Re} = 14.4$ and $C_f = 1.13$); (c) $\mathrm{Eo} = 400$ and $\mathrm{Mo} = 100$ ($\mathrm{Re} = 16.6$ and $C_f = 1.145$); and (d) $\mathrm{Eo} = 200$ and $\mathrm{Mo} = 1$ ($\mathrm{Re} = 33.8$ and $C_f = 1.30$). Insert: Bubble shape and location of the maximum interface velocity (○), maximum bubble width (◊), tip of the skirt ▽, maximum radius inside the skirt (□), and maximum interface velocity inside the skirt (∗).

for $\xi \rightarrow 0$ and $U_\xi \approx U_B r$ for $\xi \rightarrow \xi_{\max}$ where θ is the polar angle taken from the vertical axis of symmetry and r is the radial distance to the symmetry axis. The bubble shape being close to a spherical cap of radius a on the bubble front, the interface velocity U_ξ on the external bubble is described by

$$U_\xi = C_f \frac{3}{2} \sin \frac{\xi}{a} U_B, \tag{20}$$

where the coefficient C_f is used to account for the departure from the potential flow around a sphere [2]. By adjusting C_f, relation (20) is able to describe the evolution of the interface velocity on a significant part of the bubble front, almost up to the skirt beginning, as shown in Fig. 12. Note that C_f is increasing with Re due to the streamlines tightening when increasing Re.

Information provided by these simulations concerns the clarification of the velocity field structure, inside the skirt and in the gas film. The positive value for U_ξ on the internal surface of the skirt indicates that the fluids (on both the liquid and gas sides) are moving in a direction opposite to that of the external flow. This is the signature of the presence of a toroidal recirculation (see Fig. 13) that develops inside the bubble skirt with an upward vertical motion along the skirt surface and a

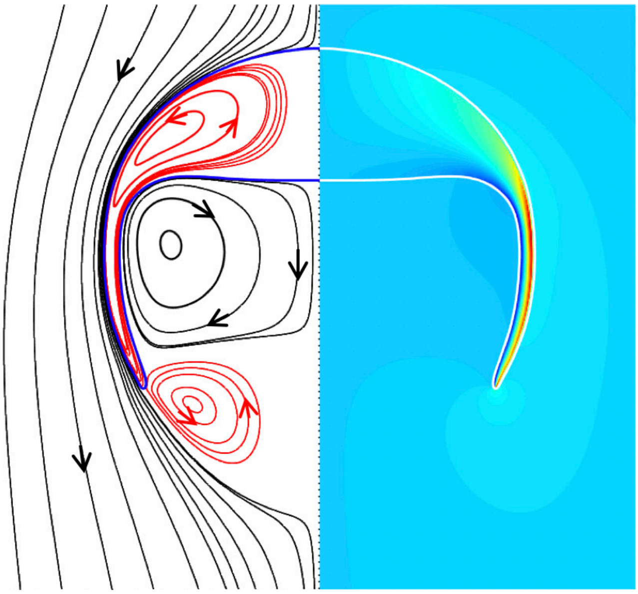

FIG. 13. Velocity field structure for the case (Eo = 330, Mo = 100): (Left) Stream lines from the numerical simulation with the identification of two toroidal vortices. (Right) Vorticity field ω ranging from the maximum value $+34.2\,U_B/R$ (in red) to the minimum value $-16.7\,U_B/R$ (in blue), both located inside the skirt film.

downward motion on the symmetry axis. Our simulations reveal that a second toroidal recirculation of opposite rotation develops below the first one and is attached at the tip of the skirt film, making the connection with the external flow. Such a velocity field structure is consistent with the numerical simulation of a skirt bubble reported by Yu and Fan [7] but clearly differs from the picture proposed by Wairegi [5] and Bhaga [2] (see also Clift *et al.* [15]) from experimental observations. Indeed, their description based on tracer trajectory proposes an single recirculation with opposite rotation inside the skirt wake, which can be consistent only with a double inflexion of the velocity field inside the skirt film corresponding to the presence of two vortices inside the skirt film. Our numerical simulations reveal a clear different velocity field organization with a single recirculation inside the bubble, but with two recirculation of opposite direction in the skirt wake. Possible explanations of this major difference can be proposed. First, only the second recirculation has been visualized in the experiment. A second reason may be due to the use in the experiments of tracer particles having size of the same order of magnitude as the skirt width as well as the suspected presence of surfactants explaining the observation of stagnation regions inside the skirt by Wairegi [5]. Note that these experiments were conducted many years ago, without access to modern PIV technics.

Figure 13 also reports the vorticity field that develops around and inside the bubble. As shown the vorticity inside the skirt film $\omega_{\mathrm{film}} = O[U_B/(\delta/2)]$ is of much larger magnitude than the vorticity that develops on the bubble surface of magnitude $\omega_{\mathrm{ext}} = O(U_B/R)$, a direct consequence of the thin film thickness δ much smaller than the bubble size. Indeed for the case reported in Fig. 13, $\delta/R \approx 0.08$ resulting in $\omega_{\mathrm{film}} \approx 25\,U_B/R$ in agreement with the values reported in the figure.

In order to provide a complete picture of the velocity field in the skirt wake and the gas film, velocity profiles are reported in Fig. 14 for both the vertical downward velocity u and the radial velocity v as a function of the radial position r to the symmetry axis (see insert of Fig. 14 for definitions). The profile of u clearly confirms the direction of rotation of the fluid circulation inside the skirt wake. Inside the skirt wake, the velocity profile is compared to the Hill's spherical vortex velocity profile $u/U_W = -(1 - 2r^2/R_W^2)$ where U_W is the local interfacial velocity inside the skirt

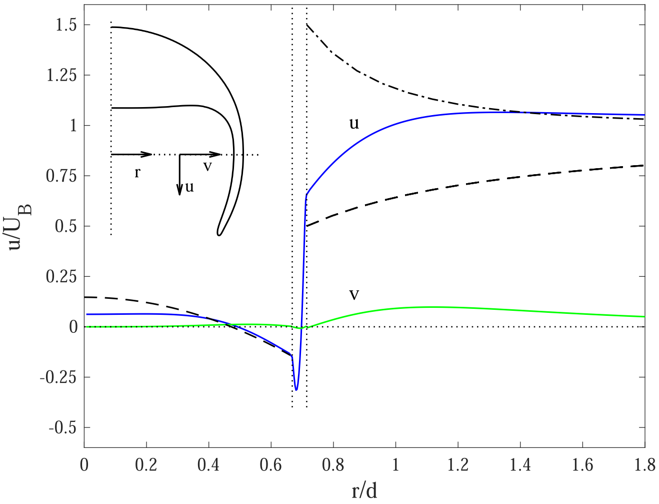

FIG. 14. Velocity profile for the vertical downward u (blue line) and radial v (green line) velocity components along the dash line shown in the insert as a function of the radial distance r for $\mathrm{Eo} = 330$ and $\mathrm{Mo} = 100$. External flow ($r/d \geqslant 0.73$): $- \cdot -$ potential solution for u, $- - -$ Hadamard-Rybczynski solution for u. Flow inside the skirt ($r/d \leqslant 0.67$): $- - -$ spherical Hill vortex solution for u.

and R_W the skirt internal radial distance. As shown the evolution is relatively in good agreement with the Hill's vortex close to the interface, but a significant deviation is observed near the symmetry axis.

Considering the liquid motion around the bubble, the velocity profile is compared both to the potential profile $u/U_B = 1 + R_S^3/(2r^3)$ and to the Hadamard-Rybczynski profile $u/U_B = 1 - R_S/(2r)$ that develop on the equator of a sphere of radius R_S where R_S is here the local radius of the bubble external surface. As expected, the interfacial velocity is overestimated by the potential flow (limit for $\mathrm{Re} \to \infty$) and is underestimated by the Hadamard-Ribzinski solution (limit for $\mathrm{Re} \to 0$) in agreement with the Reynolds number $\mathrm{Re} = 14.4$ of the considered case. Finally, we can notice that the velocity profile reported in Fig. 14 supports the assumption usually made for the skirt film modeling, i.e., a parallel flow inside the skirt film where the transverse velocity v is clearly much smaller than the longitudinal velocity u.

We define by U_S (resp. U_W) the external (resp. internal) tangential velocity on the skirt film surface, both defined positive in the ξ direction (see Fig. 1). Considering the evolution of U_ξ reported in Fig. 12, U_S and U_W significantly vary all along the skirt interface for all the cases, and both present a maximum value close to the skirt onset. The values of the maximum interfacial velocity outside the bubble $U_{S,\max}$ and inside the skirt $U_{W,\max}$ are reported in Fig. 15 for all the skirt bubbles. Both velocities are observed to increase with the bubble Reynolds number. $U_{S,\max}$ is found to be of the same order of magnitude as the bubble rising velocity U_B, ranging from $0.62\,U_B$ at smaller Reynolds numbers to $0.85\,U_B$ at larger Reynolds number. The plot indicates that the maximum interfacial velocity $U_{W,\max}$ inside the skirt is found to be significantly less than the maximum interfacial velocity $U_{S,\max}$ on the external interface. More precisely, $U_{W,\max}$ is varying from $0.08\,U_{S,\max}$ to $0.35\,U_{S,\max}$ when increasing Re, corresponding to $0.05\,U_B$ and $0.3\,U_B$, respectively.

The shape of the skirt bubble front being close to a spherical cap, the maximum external velocity is compared to the maximum velocity reported for a spherical bubble [27] written under the form

$$U_{S,\max}^{\text{sph.bubble}} = \left(\frac{1}{2} + f(\mathrm{Re})\right) U_B \quad \text{with} \quad f(\mathrm{Re}) = \frac{\mathrm{Re}}{16 + 3.315\mathrm{Re}^{1/2} + \mathrm{Re}} \tag{21}$$

in order to show the limit $1/2$ for $\mathrm{Re} \to 0$. As shown in the figure, the external maximum interfacial velocity $U_{S,\max}$ follows a close evolution but is found to be less than the maximum velocity observed

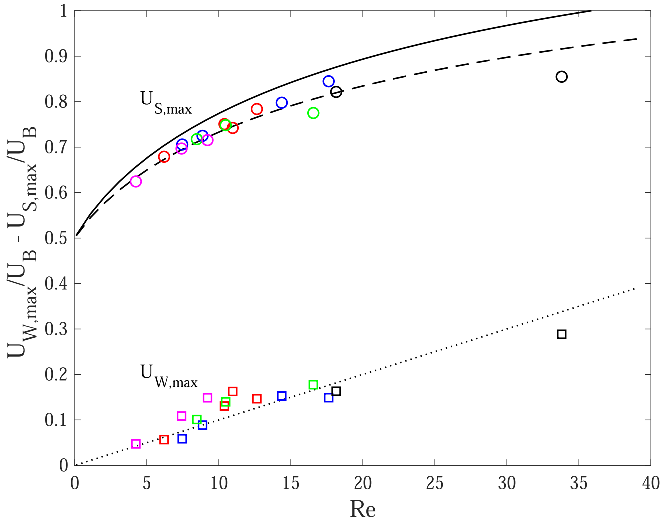

FIG. 15. Maximum interfacial velocity $U_{S,\max}$ and $U_{W,\max}$ outside and inside the skirt, respectively. The corresponding collocation are reported in the insert of Fig. 12 using symbols ○ and $*$, respectively. Black ☐ and ○ Eo = 200; blue ☐ and ○ Eo = 331; green ☐ and ○ Eo = 400; red ☐ and ○ Eo = 500; magenta ☐ and ○ Eo = 750. — Maximal tangential velocity at a spherical bubble interface from [27] given by Eq. (21).

for a spherical bubble. This velocity reduction maybe attributed to an additional viscous dissipation induced by the fluid circulation inside the skirt and transmitted through the viscous shear stress continuity on both side of the skirt interface. The evolution of the maximum interfacial velocity inside the skirt $U_{W,\max}$ is found to be linear with the Reynolds number. Finally, the evolution for $U_{S,\max}$ and $U_{W,\max}$ can be simply described by

$$U_{S,\max} = [1/2 + 0.85 f(\mathrm{Re})]\, U_B, \tag{22}$$

$$U_{W,\max} = 0.01\, \mathrm{Re}\, U_B, \tag{23}$$

as shown in Fig. 15.

B. Skirt thickness and velocity profile

Different models have been proposed for the skirt film description, and several assumptions were made in order to be able to propose a tractable model for the film thickness δ. First of all, δ is considered small compared to the skirt radius R_S to be able to neglect curvature effect so that the velocity can be considered parallel inside the skirt film [5]. This is the case for the set of skirt bubbles simulated here where δ/R_S is found to be less than 0.11. As a consequence a parallel flow develops inside the skirt as shown in Fig. 16, where the profiles for the velocity component u (resp. v) in the x direction (resp. y direction) are reported at different locations along the skirt for the cases (Eo = 330, Mo = 100, Re = 14.4) and (Eo = 400, Mo = 100, Re = 16.6) as a function of y the coordinate along the direction normal to the skirt interface as defined in Fig. 1.

Under the condition of parallel flow inside the skirt film, the velocity profile results from the momentum balance along the film direction x:

$$\mu_B \frac{d^2u}{dy^2} = A, \tag{24}$$

where $A = dp_G/dx - \rho_B g$ stands for the driving effects in the skirt film. We solve this equation considering that the local velocity on the outer side of the skirt is $u(y = \delta) = U_S$ while the velocity on

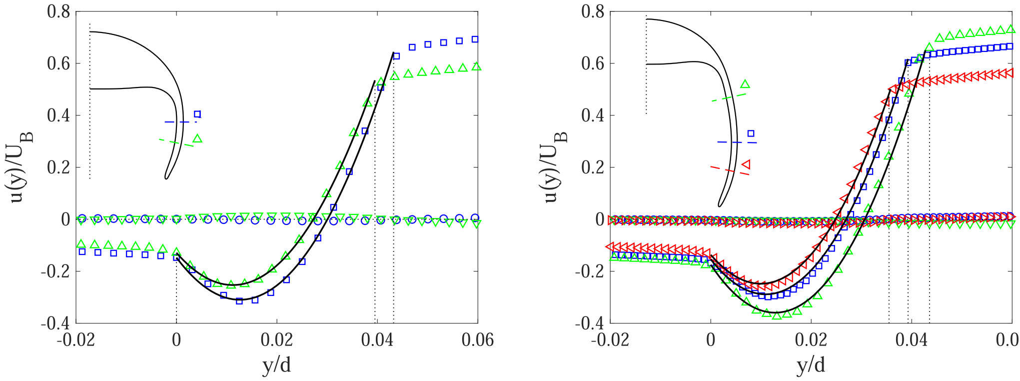

FIG. 16. Downward velocity in gas film $u(y)$ along the cross section indicated in the insert. (Left) Eo = 330 and Mo = 100. (Right) Eo = 400 and Mo = 100. — velocity profiles from Eq. (28) where the numerical values for δ, U_W, and U_S are considered.

the inner side is $u(y=0) = -U_W$ (the minus sign is the consequence of the x direction opposite to the interface curvilinear coordinates ξ inside the skirt as defined in Fig. 1). The resulting parabolic velocity profile inside the skirt film can then be expressed as

$$u(y) = \frac{A}{2\mu_B} y(y-\delta) + \frac{y}{\delta}(U_S - U_W) + U_W. \tag{25}$$

By requiring that there is no net mass transport inside the skirt film,

$$\int_0^\delta u(y)\, dy = 0, \tag{26}$$

the film thickness is

$$\delta = \sqrt{\frac{6\mu_B(U_S - U_W)}{A}}. \tag{27}$$

Replacing A in Eq. (25) we get the velocity profile expressed with the velocities U_W and U_S and the skirt thickness δ:

$$u(y) = 3(U_S - U_W)\frac{y}{\delta}\left(\frac{y}{\delta} - 1\right) + \frac{y}{\delta}(U_S + U_W) - U_W. \tag{28}$$

The velocity profile given by Eq. (28) is compared to numerical profiles in Fig. 16 in different regions of the skirt. As shown, a parabolic profile clearly connects the interfacial velocities U_S and U_W that develop on both side of the skirt film.

According to the evolutions of U_S and U_W reported in Fig. 12 [the red and green lines of $U(\xi)$, respectively], $U_S - U_W$ is decreasing along the skirt interface so that from Eq. (27), the skirt thickness is also decreasing along the skirt. This is confirmed in Fig. 17 where the evolution of the skirt thickness $\delta(\xi)$ measured in the simulations is reported as a function of ξ taken on the external surface of the skirt. The skirt continuously thins downstream: $\delta(\xi)$ first decreases, then a plateau characterized by a nearly constant skirt is observed, and finally the skirt thickness rapidly tends to zero at the skirt tip. Note that the skirt has to be long enough to observe a plateau, and for short skirt [see Fig. 17(a)] the plateau is not developped.

According to relation (27), the skirt thickness evolution is also dependent on the evolution of $A = dp_G/dx - \rho_G g$. The pressure gradient evolution inside the skirt film dp_G/dx is linked by the normal momentum balance at the interface to the pressure and viscous stress evolutions in the external fluid on both sides of the skirt film. In the skirt models proposed in the literature, the dominant contribution from the external fluid is usually assumed to be the hydrostatic pressure

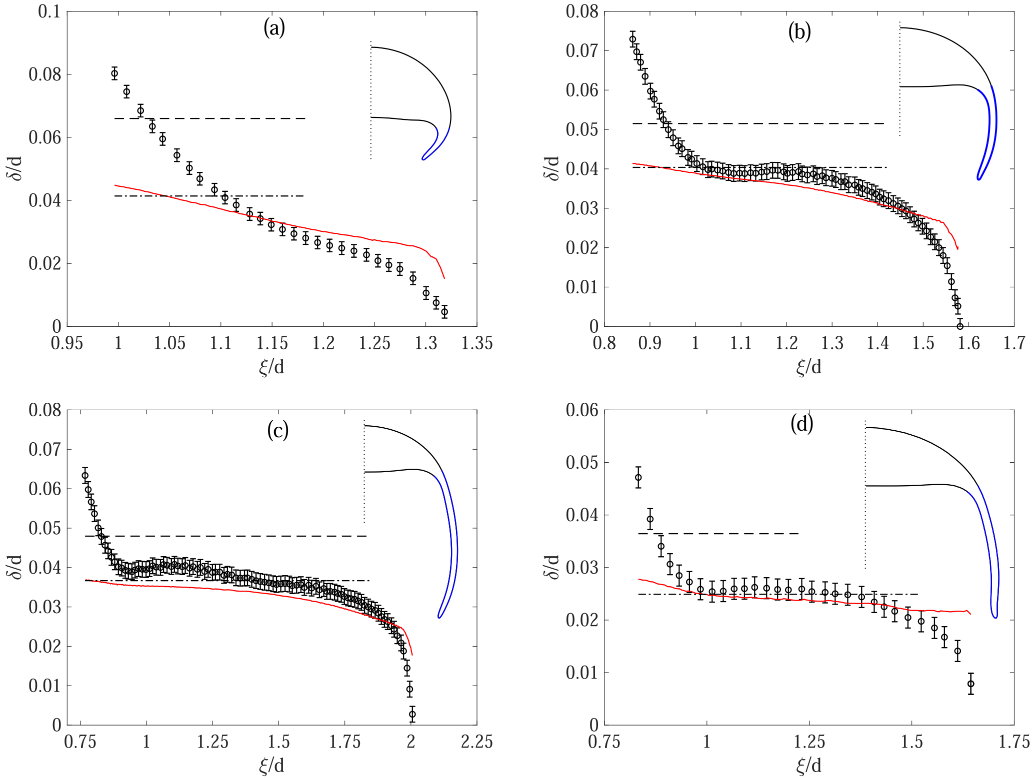

FIG. 17. Evolution of the skirt thickness δ as a function of the curvilinear coordinate ξ for (a) $\mathrm{Eo} = 500$, $\mathrm{Mo} = 5000$; (b) $\mathrm{Eo} = 330$, $\mathrm{Mo} = 100$; (c) $\mathrm{Eo} = 400$, $\mathrm{Mo} = 100$; and (d) $\mathrm{Eo} = 200$, $\mathrm{Mo} = 1$. −− relation (29) ($A^* = 1$, $U_S^* = 1$, $U_W^* = 0$); − · − relation (31) ($A^* = 1$, $U_S^* = U_{S,\max}/U_B$, $U_W^* = U_{W,\max}/U_B$); and — relation (30) ($A^* = 1$, $U_S^* = U_S(\xi)/U_B$, $U_W^* = U_W(\xi)/U_B$). An error bar corresponding to the grid size is shown because the fluid properties (and in particular the viscosity) are spread at the interface other one grid cell on both side of the interface reducing the effective gap available for the gas flow.

around the bubble [2–5] so that $dp_G/dx \approx dp_L/dx \approx \rho_L g$ and $A \approx \rho_L g$. In addition, considering at first order that the external velocity can be assumed to be close to the bubble rising velocity $U_S \approx U_B$ and that the velocity inside the skirt is much smaller than the velocity on the external surface $U_W \approx 0$, we recover the first model for the skirt thickness attributed to Guthrie [3,4] and then revisited by Wairegi [5] and Bhaga [2]:

$$\delta^G = \sqrt{\frac{6\mu_B U_B}{\rho_L g}}. \tag{29}$$

Note that a film thickness description in the case of a recirculating wake is also proposed considering $U_W \approx -U_B$, but in contradiction with the effective direction of rotation of the wake inside the skirt as discussed previously (see Fig. 13). Relation (29) is reported in Fig. 17. A correct order of magnitude is found, but relation (29) overestimates the film thickness measured in the simulations. Bhaga [2] proposed to improve this modeling by considering the departure of sphericity of the bubble (prolate and oblate) and the development of the flow around the bubble. In addition to the parameter C_f introduced to correct for the deviation from potential flow around a sphere [see Eq. (20)], an additional parameter F is introduced to reproduce the thinning of the skirt along the skirt film. Ray and Prosperetti [6] accounted for the viscous boundary layer on the outer side of the bubble. As

TABLE II. Overview of the skirt thickness expressions from the literature.

Reference	A^*	U_S^*	U_W^*	Approximations
Guthrie *et al.* [3,4]	1	1	0	Stagnant wake relation (29)
Wairegi [5]	1	1	-1	Recirculating wake
Bhaga [2]	$1/F^2$	C_f	0	Stagnant wake
	$1/F^2$	C_f	$-C_f$	Recirculating wake
Rai and Prosperetti [6]	1	$U_S(\xi)/U_B$	0	Boundary-layer-type correction
This study	1	$U_{S,\max}/U_B$	$U_{W,\max}/U_B$	Expressions deduced from simulation and given by relations (22) and (23)

shown by the authors, this consideration causes the skirt to thin downstream. To help comparison of the proposed modeling, relation (27) is rewritten under the form

$$\delta = \delta^G \sqrt{\frac{1}{A^*}} \sqrt{U_S^* - U_W^*}, \tag{30}$$

where $A^* = A/\rho_L g$, $U_S^* = U_S/U_B$, and $U_W^* = U_W/U_B$. Table II summarizes the expressions considered for A^*, U_S^*, and U_W^* in the skirt thickness expressions found in the literature when considering a gas bubble.

Depending on the relative effect of inertia and viscosity in the external liquid and how they compare to the hydrostatic pressure effect at the bubble scale, a Re correction can be expected. For the skirt bubbles considered here, inertia to hydrostatic pressure ratio U_B^2/gd ranges between 0.1 and 0.4, while viscous stress to hydrostatic pressure ratio $\mu_L U_B/\rho_L g d^2$ ranges between 0.01 and 0.045. Thus, hydrostatic pressure dominates, and in a first attempt to describe the film thickness, we can consider $A^* \approx 1$ ($A \approx \rho_L g$). Then the local values of both $U_S(\xi)$ and $U_W(\xi)$ obtained from the simulation are considered in relation (30). The corresponding evolution is shown in Fig. 17. The agreement with the numerical results is clearly improved, and the film thickness decrease is correctly reproduced except close to the tip. In order to provide an estimate of the skirt plateau value δ_P, we propose $U_{S,\max}$ (resp. $U_{W,\max}$) as the characteristic velocity for the external (resp. internal) interfacial skirt velocity:

$$\delta_P = \sqrt{\frac{6\mu_B(U_{S,\max} - U_{W,\max})}{\rho_L g}}. \tag{31}$$

The corresponding value is reported in Fig. 17 and a very good agreement is observed with the plateau value when observed. Only one experimental skirt film thickness measurement is available in the literature when considering a skirt bubble, i.e., a fluid particle satisfying the conditions $\mu_B/\mu_L \ll 1$ and $\rho_B/\rho_L \ll 1$. Experimental measurement using an optical system is challenging due to the very small thickness of the film and induced reflections. Indeed, considering typical values for skirt bubble $d = O(1)$ cm, $U_B = O(50)$ cm/s, $\rho_L = O(10^3)$ kg/m^3, and $\mu_B = O(2 \times 10^{-5})$ Pa s, the expected order of magnitude of the film thickness from relations (29) and (31) is $\delta = O(50)$ μm. Guthrie and Bradshaw [4] developed an original experimental method to determine the skirt thickness by cutting the bubble with a thin steel plate across the upper section of the column. A series of ten experiments is reported for a $d = 4.66$ cm nitrogen bubble rising in glycerol, and a value of 41 ± 8 μm is obtained for δ. It is compared in Table III with relation (29) [3,4] and relation (31) based on our numerical simulations. As shown both relations give the same order of magnitude. While relation (29) overestimates the experimental value, it is remarkable that relation (31) gives a very good estimate of the experimental value and clearly improves the original expression. The use of the effective velocities $U_{S,\max}$ and $U_{W,\max}$ on both sides of the interface as characteristic velocities clearly improves the prediction and satisfactorily accounts for both the

TABLE III. Comparison of the skirt thickness from relations (29) and (31) with experiment from Guthrie and Bradshaw [4] for a nitrogen bubble in glycerol.

U_B (cm/s)	d (cm)	μ_L (Pa s)	ρ_L (kg/m^3)	μ_B (Pa s)	δ experiment (μm)	δ relation (29) (μm)	δ relation (31) (μm)
34	4.66	1.23	1260	1.76×10^{-5}	41 ± 8	54	43

Reynolds and shape correction. Thus, considering relations (22) and (23) proposed for $U_{S,\max}$ and $U_{W,\max}$, respectively, the following description of the skirt thickness is proposed:

$$\delta_P = \delta^G \,\mathrm{sk}(\mathrm{Re}), \tag{32}$$

where the Guthrie expression for the skirt thickness is corrected with the Re function $\mathrm{sk}(\mathrm{Re}) = 1/2 + f(\mathrm{Re}) - 0.01\mathrm{Re}$ with $f(\mathrm{Re})$ given in Eq. (21). This relation is compared in Fig. 18 to the numerical results and the experimental value of Guthrie and Bradshaw [4]. As shown the agreement is very good. In particular, a maximum observed around $\mathrm{Re} = 15$ is described with this relation. The difference is larger when considering a curved skirt compared to a vertical skirt, suggesting an additional correction due to the skirt curvature. This plot also indicates that the relation proposed by Guthrie gives a good order of magnitude for all the reported simulations. Indeed, the skirt thickness plateau normalized by δ^G is observed to be nearly constant,

$$\delta_P \approx 0.75\,\delta^G, \tag{33}$$

providing a good estimation of the thickness of a bubble skirt.

C. Skirt length

The skirt length ℓ normalized by the bubble diameter d is reported in Fig. 19. The numerical simulations are compared with the experiments reported for bubbles by Bhaga [2]. The reported experimental skirt lengths are deduced from the tracing of skirt bubbles deduced from their

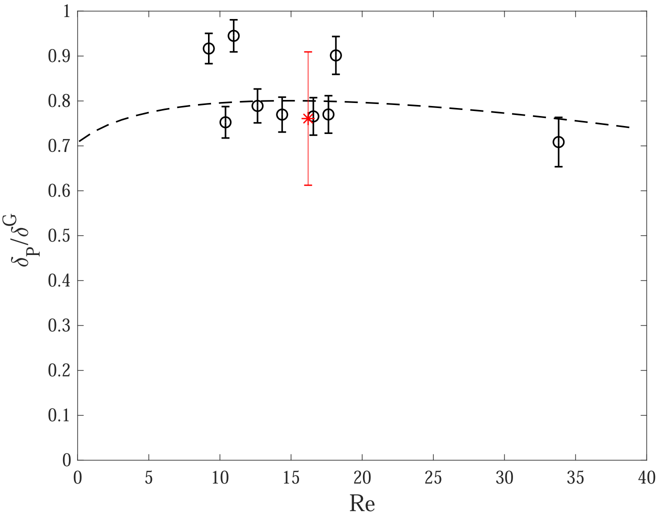

FIG. 18. Evolution of the skirt thickness plateau δ_P normalized by δ^G as a function of Re. ○ numerical simulation, $*$ mean value from the ten experiments of Guthrie and Bradshaw [4], — — — $\mathrm{sk}(\mathrm{Re}) = 1/2 + f(\mathrm{Re}) - 0.01\mathrm{Re}$ from relation (32).

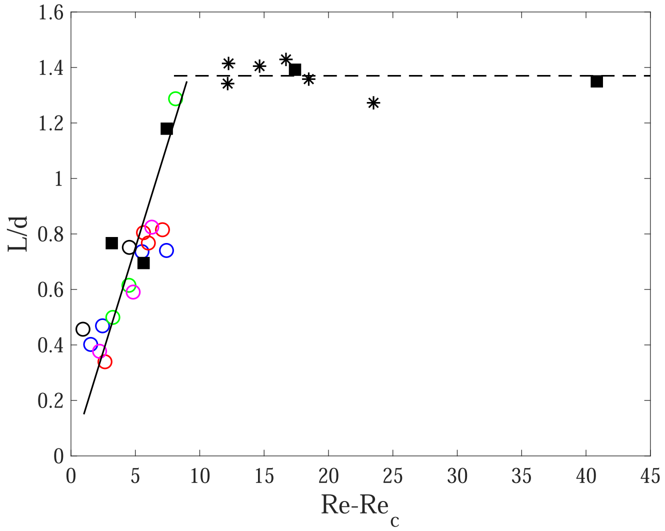

FIG. 19. Evolution of the normalized skirt length ℓ/d as a function of $\mathrm{Re}-\mathrm{Re}_c$. For numerical simulation Re_c is given by $\mathrm{Re}_c = 70/\mathrm{Ca}$, while for experiments it is deduced from Fig. 6.9 in [2]. Numerical results: black ○ Eo = 200; blue ○ Eo = 331; green ○ Eo = 400; red ○ Eo = 500; magenta ○ Eo = 750. $*$ Skirt length at the instability development for unstable cases (from Fig. 8); ■ experiments from [2]; — relation (34); $--$ $\ell = 1.37d$.

experimental observations [from their Fig. 3.4(b)]. Note that Wairegi [5] also reports a series of measurement of bubble skirt length, but, unfortunately, the provided information does not make possible the use of these data. The evolution of the normalized skirt length ℓ/d has been plotted as a function of the Weber number We, capillary number Ca, or Reynolds number Re (not shown here). The best representation is obtained with a plot first suggested by Wairegi [5] that consists in reporting the normalized skirt length ℓ/d as a function of $\mathrm{Re}-\mathrm{Re}_c$ where Re_c is the Reynolds number corresponding to the onset of the skirt, the capillary number being fixed. According to Fig. 6, $\mathrm{Re}_c = 70/\mathrm{Ca}$ for the simulated skirt bubbles. The skirt threshold for the experiments is determined in the same way (deduced from Fig. 6.9 in Bhaga [2]). As shown in Fig. 19, both experiments and simulations are collapsing on a very consistent evolution revealing two regimes. For values of $\mathrm{Re}-\mathrm{Re}_c$ smaller than 10, the skirt length evolves roughly linearly with the deviation from threshold Re_c and can be described by

$$\frac{\ell}{d} = 0.15(\mathrm{Re} - 70/\mathrm{Ca}). \tag{34}$$

For larger deviation from the threshold, i.e., for $\mathrm{Re}-\mathrm{Re}_c \geqslant 10$, a plateau seems to be observed corresponding to a constant value

$$\ell \approx 1.37d \tag{35}$$

when increasing the Reynolds number. This suggests that a skirt length larger than the limit corresponding to relation (35) cannot be observed. If the skirt becomes longer during its formation due to the entrainment by the surrounding flow, the skirt starts to be unstable, and then its size is reduced by fragmentation. This proposition is confirmed by reporting in the figure the value of the skirt length when the skirt instability starts to develop for the unstable cases (see Fig. 8). These values are in very good agreement with the plateau $\ell = 1.37d$. The skirt instability is certainly observed when the skirt length reaches the wave length of the first unstable mode. Additional experiments as well as an appropriate stability analysis of the gas skirt film should be conducted in order to discuss if the more unstable wave length is consistent with condition (35).

VI. CONCLUSIONS

The aim of this work was to conduct an investigation of skirt bubble when rising in a viscous liquid. Covering the range of Eötvös number where they can be observed, direct numerical simulations were conducted to provide a detailed description of the skirt bubble dynamics (terminal velocity and drag), the flow field organization (inside the skirt film, around the bubble, and inside the gas film that forms the skirt) as well as their geometrical characteristics (both skirt length and thickness). First, a unified relation for the terminal velocity (and drag force) has been provided for bubbles (dimple, skirt, and spherical cap bubbles) when considering Eötvös numbers larger than 100. Then we have described the parallel Poiseuille flow that develops inside the skirt film and characterized the interfacial velocities on both sides of the skirt film. The simulations outline that the liquid velocity on the outer side of the skirt differs from the bubble rising velocity and that the velocity inside the skirt has a much smaller magnitude. As a major result obtained from the simulation, we show that only one recirculation is observed inside the bubble while two toroidal vortices develop in the skirt wake, a clear difference with the picture deduced from experimental observations. Another significant contribution of this work concerns the skirt thickness and length. First, we show that the original relation $\delta^G = \sqrt{6\mu_B U_B/\rho_L g}$ proposed by Guthrie [3] and Guthrie and Bradshaw [4] can be used to provide a good estimate of the skirt thickness plateau $\delta_P \sim 0.75\,\delta^G$. Based on our numerical simulations we propose a Reynolds correction considering the maximum velocities observed on both sides of the skirt film interface. This provides a prediction in very good agreement with the only one experimental value reported by Guthrie and Bradshaw [4] for a $d = 4.66$ cm nitrogen bubble rising in glycerol. Considering the skirt length, our simulations combined with experimental observations suggest the existence of a maximum value for the skirt length $\ell \approx 1.37d$. Three-dimensional simulations can now be conducted to investigate the transition from stable to unstable skirt and the resulting skirt length limit suggested by both our simulation and experiments. Conducting accurate experiments is also needed to validate our results in particular concerning the recirculation inside the skirt and the skirt shape characteristics.

ACKNOWLEDGMENT

The author would like to thank Mostafa Sulaiman, who did some preliminary simulations of skirt bubbles with VoF@JADIM.

[1] J. Thomson and H. Newall, On the formation of vortex rings by drops falling into liquids, and some allied phenomena, Proc. R. Soc. London **39**, 417 (1885).

[2] D. Bhaga, Bubbles in viscous liquids: Shapes, wakes and velocities. Ph.D. thesis, McGill University, 1976.

[3] R. I. L. Guthrie, Dynamic and MAS transfer phenomena of spherical capped bubble, Ph.D. thesis, Imperial College, 1967.

[4] R. I. L. Guthrie and A. V. Bradshaw, The stability of gas envelopes trailed behind large spherical cap bubbles rising through viscous liquids, Chem. Eng. Sci. **24**, 913 (1969).

[5] T. Wairegi, The mechanics of large bubbles and drops moving through extended liquid media, Ph.D. thesis, McGill University, 1974.

[6] B. Ray and A. Prosperetti, On skirted drops in an immiscible liquid, Chem. Eng. Sci. **108**, 213 (2014).

[7] Z. Yu and L.-S. Fan, Direct simulation of the buoyant rise of bubbles in infinite liquid using level set method, Can. J. Chem. Eng. **86**, 267 (2008).

[8] M. Ohta and M. Sussman, The buoyancy-driven motion of a single skirted bubble or drop rising through a viscous liquid, Phys. Fluids **24**, 112101 (2012).

[9] T. Bonometti and J. Magnaudet, An interface capturing method for incompressible two-phase flows. validation and application to bubble dynamics, Int. J. Multiphase Flow **33**, 109 (2007).

[10] J. Hua and J. Lou, Numerical simulation of bubble rising in viscous liquid, J. Comput. Phys. **222**, 769 (2007).

[11] J. Hua, J. F. Stene, and P. Lin, Numerical simulation of 3D bubbles rising in viscous liquids using a front tracking method, J. Comput. Phys. **227**, 3358 (2008).

[12] S. Hysing, S. Turek, D. Kuzmin, N. Parolini, E. Burman, S. Ganesan, and L. Tobiska, Quantitative benchmark computations of two-dimensional bubble dynamics, Int. J. Numer. Methods Fluids **60**, 1259 (2009).

[13] S. O. Unverdi and G. Tryggvason, A front-tracking method for viscous, incompressible, multi-fluid flows, J. Comput. Phys. **100**, 25 (1992).

[14] M. K. Tripathi, K. C. Sahu, and R. Govindarajan, Dynamics of an initially spherical bubble rising in quiescent liquid, Nat. Commun. **6**, 6268 (2015).

[15] R. Clift, J. R. Grace, M. E. Weber, *Bubbles, Drops and Particules* (Academic Press, New York, 1978).

[16] T. Abadie, J. Aubin, and D. Legendre, On the combined effects of surface force calculation and interface advection on spurious currents within volume of fluid and level set frameworks, J. Comput. Phys. **297**, 611 (2015).

[17] O. Atasi, B. Haut, A. Pedrono, B. Scheid, and D. Legendre, Influence of soluble surfactants and deformation on the dynamics of centered bubbles in cylindrical microchannels, Langmuir **34**, 10048 (2018).

[18] O. Atasi, D. Legendre, B. Haut, R. Zenit, and B. Scheid, Lifetime of surface bubbles in surfactant solutions, Langmuir **36**, 7749 (2020).

[19] J. Dupont and D. Legendre, Numerical simulations of static and sliding drop with contact angle hysteresis, J. Comput. Phys. **229**, 2453 (2010).

[20] M. Sussman, E. Fatemi, P. Smerecka, and S. Osher, An improved level set method for incompressible two-phase flows, Comput. Fluids **27**, 663 (1998).

[21] R. M. Davies and G. Taylor, The mechanics of large bubbles rising through extended liquids and through liquids in tubes, Proc. Roy. Soc. A **200**, 375 (1950).

[22] T. Taylor and A. Acrivos, On the deformation and drag of a falling viscous drop at low Reynolds number, J. Fluid Mech. **18**, 466 (1964).

[23] J. S. Hadamard, Mouvement permanent lent d'une sphere liquide et visqueuse dans un liquide visqueux, C. R. Acad. Sci. Paris **152**, 1735 (1911).

[24] W. Rybczynski, On the translatory motion of a fluid sphere in a viscous medium, Bull. Acad. Sci., Cracow, Series A, 40 (1911).

[25] J. Cano-Lozano, R. Bolanos-Jimenez, C. Gutierrez-Montes, and C. Martinez-Bazan, The use of volume of fluid technique to analyze multiphase flows: Specific case of bubble rising in still liquids, Appl. Math. Model. **39**, 3290 (2015).

[26] D. Bhaga and M. Weber, Bubbles in viscous liquid: Shape, wakes and velocities, J. Fluid Mech. **105**, 61 (1981).

[27] D. Legendre, On the relation between the drag and the vorticity produced on a clean bubble, Phys. Fluids **19**, 018102 (2007).